Quantifying the mixing of trade-wind cumulus during the NEPHELAE-EUREC4A field campaign with remotely piloted aircraft

Nicolas Maury, Gregory Roberts, Fleur Couvreux, Titouan Verdu, Pierre Narvor, Simon Lacroix, Gautier Hattenberger

ORIGINAL ARTICLE

Journal Section

Quantifying thermodynamic properties and temporal evolution of trade-wind cumulus during NEPHELAE-EUREC4A field campaign with Remotely Piloted Aircrafts

Nicolas Maury†[1] | Gregory C. Roberts[1,2] | Fleur Couvreux[1] | Titouan Verdu[3,4] | Pierre Narvor[3] | Simon Lacroix[3] | Gautier Hattenberger[4]

[1]Centre National de Recherches Météorologiques, Université de Toulouse, Météo-France, CNRS, Toulouse, France

[2]Scripps Institution of Oceanography, University of California San Diego, La Jolla, USA

[3]Laboratoire d'Analyse et d'Architecture des Systèmes, Université de Toulouse, CNRS, Toulouse, France

[4]Ecole Nationale de l'Aviation Civile, Université de Toulouse, Toulouse, France

Correspondence
Nicolas Maury and Gregory C. Roberts
Email: nicolas.maury@lmd.ipsl.fr and greg.roberts@meteo.fr

Present address
†LMD/IPSL, Sorbonne Université, CNRS, Paris, 75005, France

Funding information
Agence Nationale de la Recherche (Project-ANR-17-CE01-0003), Aerospace Valley and Météo-France

Cumulus clouds, in spite of their small size, have an important impact on the terrestrial radiation balance because of their large coverage, especially over the subtropical region. The characterisation of their temporal evolution remains a challenge for their observation, as cumulus clouds have short lifetimes. A new sampling strategy using Remotely Piloted Aircraft (RPA) was implemented during the NEPHELAE-EUREC[4]A field campaign in January and February 2020 in Barbados. The 40 flights made it possible to characterize the thermodynamic transects of forced and active trade-wind cumulus clouds. The statistics show that large clouds (transect length greater than 500 m) have a core associated with positive buoyancy, high liquid water values, and an envelope associated with negative buoyancy. Small clouds with a transect length less than 500 m are generally forced cumuli since their buoyancy remains negative. The novel sampling strategy uses sensor-driven adaptive sampling to autonomously track an individual cloud throughout its lifetime. In-situ observations of the cloud properties and its surrounding environment also show that turbulence

mixing is underestimated by a high-resolution Large-Eddy Simulation.

KEYWORDS
adaptive sampling, observations, Remotely Piloted Aircraft, trade-wind cumulus clouds, observation, entrainment mixing

1 | INTRODUCTION

Cumulus clouds are small clouds, on the order of a kilometer, and they aggregate in privileged zones, notably in trade wind regimes where the cloud cover can reach 50%. The understanding of the evolution of cumulus clouds during their life cycle is therefore important for representing their radiative effect in numerical simulations.

The traditional sampling strategy using in-situ observations consists of transecting the cumulus clouds with research aircraft (Stevens et al. (2003), Rauber et al. (2007), Roberts et al. (2008), Burnet and Brenguier (2010)). Studies such as Katzwinkel et al. (2014) have shown that cumulus clouds are composed of a core, associated with updrafts and elevated values of liquid water content (LWC), and an envelope surrounding the cloud, composed of downdrafts, that compensate for the upward mass flux of core. As described by Hoffmann et al. (2014), single transects in cumulus clouds tend to overestimate the total water content of the cumulus core. Also, a transect through a cloud only captures a given instant of the cloud's life cycle. Yet climate models attempt to represent the impact of the whole population of cumulus clouds, which include clouds in their development, mature and dissipation phases. Katzwinkel et al. (2014) shows that thermodynamic properties of the clouds change during each of these three phases of the cloud life cycle. In the development phase, the almost entire cloud volume is defined by an ascending core and a thin subsiding envelope. The clouds in the mature and dissipation phases are composed mainly of air masses with negative buoyancy, associated with downdrafts resulting in a decrease in LWC.

In the last decades, traditional piloted research aircraft have observed the temporal evolution of a horizontal section of cloud (Burnet and Brenguier (2007)). However, piloted research aircraft remain a limited means to follow a cloud semi-continuously, as they require several minutes to return to the same cloud allowing only two or three transects before the cloud dissipates (Barnes et al. (1996)). Mallaun et al. (2018) deployed a research aircraft during a measurement campaign and achieved three to four transects of the same cloud element at different cloud levels. They observe the subsiding shell at different vertical levels and the dispersion of updrafts inside the cumulus cloud, but could not describe its temporal evolution.

To compliment the challenge of studying atmospheric phenomena in four dimensions, large eddy simulations (LES) explicitly model shallow convention and have proven to be useful to understand the main processes involved in cumulus clouds (Neggers et al. (2003), Heus and Jonker (2008)). LES have thus become a central tool in the development of parameterizations for regional and global models. LES, in turn, include sub-grid parameterizations such as turbulence and cloud microphysical parameterizations which also introduce model uncertainties. The validation of the LES simulations is often done by comparison to in-situ observations from measurement campaigns, in particular to those measuring the macroscopic and thermodynamic properties of cumulus clouds (Brown et al. (2002), Siebesma et al. (2003), Zhang et al. (2017)). However, some subgrid processes, such as microphysical and fine-scale turbulence, are parameterized and are sources of uncertainties in the representation of shallow cumulus.

As observations are still needed to refine these sub-grid parameterizations, a new approach to observing with a higher spatial and temporal resolution has been developed using Remotely Piloted Aircraft (RPA) by coupling sensors

with the autopilot to drive adaptive sampling by detecting the cloud borders and account for advection to autonomously sample the cloud for the duration of its lifetime (Maury et al. (2022)). The motivation of the Network for studying Entrainment and microPHysics of cLouds using Adaptive Exploration (NEPHELAE) was to develop a system using RPA to follow and observe the dynamic nature of clouds. In January and February 2020, we sampled individual trade wind cumuli during the field campaign EUREC^{4}A (ElUcidating the RolE of Cloud-Circulation Coupling in ClimAte; Stevens et al. (2020)).

These in-situ RPA-based measurements are also compared with LES simulations of trade wind cumuli originating from Barbados Oceanographic and Meteorological EXperiment (BOMEX) studies (Siebesma et al. (2003), Zhao and Austin (2005a)).

Section 2 presents the instrument payload deployed during the field campaign, as well as the calibration and validation of the optical cloud and meteorological sensors on-board the RPA. Section 3 describes a statistical analysis of clouds sampled and presents the first measurements of autonomous adaptive sampling individual clouds and their temporal evolution of the microphysical and thermodynamic properties.

2 | METHODOLOGY

This section describes the instruments deployed on the RPA, the parameters that have been computed, and the strategy of exploration deployed during the field campaign. The SkyWalker-X6 is a light weight RPA, with a take-off weight of 2.5 kg and a flight time of about 1.5 hours. The Skywalker X6 has been used in previous field campaigns to study clouds and is described in Sanchez et al. (2017) and Calmer et al. (2019).

2.1 | RPA payload

The RPA scientific payload was specifically designed to measure cloud optical and thermodynamic properties and send the data directly to the GPS-based autopilot, Paparazzi (PPRZ, Hattenberger et al. (2014)). The RPA payload comprised of a cloud sensor to measure the intensity of backscattered light (Nicoll and Harrison (2012)), as well as temperature and relatively humidity probe mounted in a shielded housing designed to shed cloud droplets (Sanchez et al. (2017)). A camera was also integrated for post-flight visualization of the mission.

2.1.1 | PTU probe

The PTU probe (pressure, temperature and relative humidity, Fig 1,a) has been integrated (same payload as Sanchez et al. (2017)).

The water vapour content (q_v) has been calculated as:

$$r_v = \frac{0.622 \mathsf{p}_{\mathsf{sat}}.\mathsf{RH}}{101325 - \mathsf{p}_{\mathsf{sat}}.\mathsf{RH}} \quad ; \quad q_v = \frac{r_v}{1 + r_v}, \tag{1}$$

where RH is the relative humidity and p_{sat} is the saturated vapour pressure (in kg m^{-1} s^{-2})) defined as:

$$\mathsf{p}_{\mathsf{sat}} = \exp(23.3265 - \frac{3802.7}{\theta + 273.18} - (\frac{472.68}{\theta + 273.18})^2) \tag{2}$$

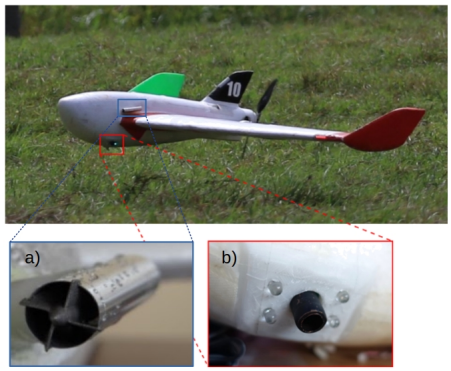

FIGURE 1 Picture of the SkyWalker-X6 RPA with a) the PTU (pressure, temperature and humidity) probe and b) the Cloud Sensor.

With the saturated vapour pressure expression, $q_{v,sat}$ can be determined as:

$$q_{v,sat} = 0.622 \frac{p_{sat}}{P - p_{sat}} \tag{3}$$

and the air is considered saturated when the measured relative humidity is above a 95% threshold (Sanchez et al. (2017)).

2.1.2 | Validation of Cloud Sensor

The Cloud Sensor, CS, directly measures the cloud optical properties to infer its cloud microphysical properties. The CS is three-wavelength cloud sensor (CS; Nicoll and Harrison (2012)) that measures extinction (Fig 1,b, Eq. 4) with a temporal resolution of 8 Hz (corresponding to a spatial resolution of approximately 2 meters based on an RPA airspeed of 15 m s^{-1}). The CS was integrated into the fuselage of the RPA facing 45 degrees downward and perpendicular to the airflow.

The CS is used to detect the presence of a cloud with four channels composed of three wavelengths (blue, λ = 505 nm; orange, λ = 590 nm; two near infra-red, λ = 840 nm). The backscatter signal is measured by the photodiode detector to determine extinction (Harrison and Nicoll (2014), Sanchez et al. (2017)). To relate entrainment mixing to a conservative variable, extinction σ_{ext}, (defined in Eq. 4) needs to be related to liquid water content (LWC).

$$\sigma_{ext} = \sum_{n=r_{min}}^{r_{max}} Q_{ext} \pi r^2 n(r) \quad ; \quad LWC = \sum_{n=r_{min}}^{r_{max}} \rho_w \frac{4}{3} \pi r^3 n(r) \tag{4}$$

where Q_{ext} is the extinction efficiency for cloud droplets, r is the radius of droplet, n(r) is the number of droplets at radius r, and ρ_w is the liquid water density.

To approximate LWC_{CS} from the CS measurement of extinction, a comparison between the CS and a FM100 (Fog Monitor 100) has been performed during the BIOMAIDO (Bio-physicochemistry of tropical clouds at Maîdo, Leriche and Colomb (2020)) campaign in La Reunion island. The FM100 measures cloud droplet size distributions between 2

and 50 μm diameter and was co-located with the CS. During a period of five days, both instruments measured the cloud microphysical properties during different meteorological conditions including slope, shallow and deep convection. The FM100 measures cloud droplet concentration and size distribution to determine LWC, which is then related to the CS measurement of extinction.

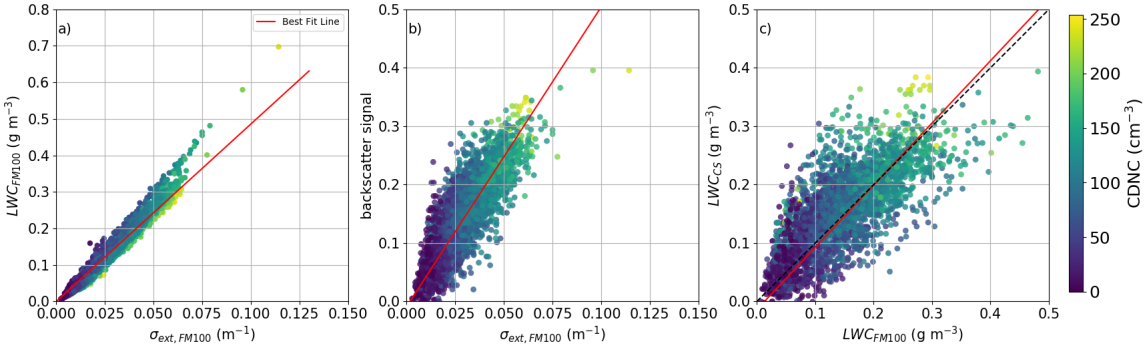

FIGURE 2 a) Comparison of LWC$_{CS}$ versus extinction calculated by FM100, b) Comparison of Cloud Sensor backscatter signal versus extinction calculated by FM100 and c) Comparison of LWC$_{CS}$ calculated by Cloud sensor versus by FM100. The dotted black and red line corresponds to 1:1-correspondence and best fit line, respectively. The colorbar represents the cloud droplet number concentration (CNDC).

Figure 2,a shows the values obtained by FM100 for extinction and LWC$_{CS}$ during the BIOMAIDO campaign as a function of color-coded cloud droplet concentrations. The LWC$_{CS}$ can be approximated empirically from the FM100 measurements by $LWC = 4.54\sigma_{ext}$ (R^2=0.99). Figure 2,b describes the CS backscatter signal with FM100 extinction as $\sigma_{ext,CS}$ = 0.336 $\sigma_{ext,FM100}$ (R^2 =0.81). For this study, the LWC$_{CS}$ is between 0.01 (detection threshold of CS) and 0.7 g m^{-3}, based on a range of effective radii between 3 and 12 micrometers. The LWC$_{CS}$ derived by the CS (LWC$_{CS}$) and the LWC$_{CS}$ measured by FM100 show an linear relationship as shown in Fig. 2,c (slope=1.06, R^2=0.76). The magnitude of LWC$_{CS}$ measured at La Réunion island is within the range of LWC$_{CS}$ values observed in the tropical western Atlantic Ocean near Barbados (Gerber et al. (2008)).

2.1.3 | Determination of conservative variables

The tracking of total water content (q_t) throughout the life cycle of the cumulus cloud quantifies the past exchanges (i.e., entrainment) between the cloud and its environment. Without entrainment, q_t would remain uniform and adiabatic throughout a cloud cross section.

The q_t is defined as the sum of the specific humidity, q_v, and liquid water content, q_l, by the following equation:

$$r_l = \frac{LWC}{\rho} \quad ; \quad q_l = \frac{r_l}{1 + r_l} \quad ; \quad qt = q_v + q_l \tag{5}$$

where ρ represents the air density determined from temperature (T, in K) and pressure (P, in Pa).

With q_v and q_l, the virtual potential temperature, θ_v, is defined in Equation 6. The difference between the cloud virtual potential temperature ($\theta_{v,c}$) and the environment virtual potential temperature ($\theta_{v,e}$) defines the buoyancy of the cloud air, β. The environmental air is the same altitude as the cloud and beyond the region affected by the cloud (i.e., outside the shell).

$$\theta_v = \Theta(1 + (q_v(\frac{Rv}{Rd} - 1)) - q_l) \quad ; \quad \beta = 9.81\frac{\theta_{v,c} - \theta_{v,e}}{\theta_{v,e}} \tag{6}$$

where Rv is the perfect gas constant for humid air (461 m^2 K^{-1} s^{-2}) and Rd perfect gas constant for dry air (287 m^2 K^{-1} s^{-2}). A mass fraction (denoted χ) of adiabatic cloudy air at a given level, z, can be determined as :

$$\Psi c_z = \chi \Psi c_{z-1} + (1 - \chi)\Psi e_z \quad ; \quad \chi(z) = \frac{\Psi c_z - \Psi e_z}{\Psi c_{z-1} - \Psi e_z} \tag{7}$$

with Ψ representing the conservative variable, indices c and e representing the cloudy and environmental air, respectively.

2.2 | RPA measurements

The SkyWalker-X6 RPA have also been used in field campaigns in Ireland and Cyprus to study aerosol-cloud interactions (Sanchez et al. (2017), Calmer (2018), Calmer et al. (2019)). This study focuses on the analysis of flights conducted by Skywalker-X6 RPAs in the tropical western Atlantic Ocean near the northeastern coast of Barbados during the EUREC^{4}A field campaign (Stevens and Bony (2021)). The Morgan Lewis field (13.27 N, 59.57 W, 30 m above sea level) was used as the operations site (black star in Figure 3). Between 27 January and 9 February 2020, 42 research flights were conducted (see Table 1, Fig. 3). The authorized airspace had a trapezoidal shape extending 15 km to the east where the maximum width was 5 km. RPAs flew in the cloud layers below the maximum altitude of 1000 m asl. During the same period, flights with RAAVEN RPAs were operated by the University of Colorado as a part of the ATOMIC (Atlantic Tradewind Ocean-Atmosphere Mesoscale Interaction Campaign) project in the same vicinity, measuring turbulence in the subcloud layer (de Boer et al. (2022)).

This study focuses on the analysis of two RPAs (SkyWalker X6-7 and X6-10, Fig. 3a,b). Before every flight, the cloud base and meteorological conditions (e.g., wind speed and direction) were determined with a ceilometer and anemometer, respectively, based at Barbados Cloud Observatory (BCO; 13.09 N, 59.25 W). Also, the cloud fraction (visualized with GOES-East satellite) and cloud thickness (using reflectivity BCO radar; Hagen et al. (2021)) were used for flight planning, particularly in choosing the measurement altitude of the RPA relative to cloud base.

The research flights were divided into different strategies as follows: 19 flights consisted of racetracks perpendicular to the wind (H), five flights were dedicated to vertical profiles (P), and 18 flights focused on cloud tracking (A). For the cloud tracking flights, the RPA initiated the mission along a racetrack pattern upwind of the operation area

TABLE 1 Overview of flight parameters with flight number, date, RPA identity, takeoff and landing time, flight duration, pattern type (R for racetrack, A for adaptive sampling, and P for vertical profile) and pattern flight altitude (or maximum altitude for vertical profiles.

Flights	Date (dd/mm)	RPA ID	Take-off hh:mm (LT)	Landing hh:mm (LT)	Duration (min)	Type	altitude (m)
1	27/01	12	11:08	12:08	60	R	800
2	28/01	10	10:17	11:20	63	R	550
3	28/01	10	15:52	16:49	57	R	800
4	28/01	12	15:52	16:54	62	R	800
5	29/01	10	11:30	12:28	58	R	550
6	29/01	10	14:32	15:37	65	R	850
7	29/01	10	16:17	17:25	68	R	750
8	29/01	12	11:31	12:25	54	R	650
9	29/01	12	14:43	15:40	57	R	750
10	29/01	12	16:17	17:27	70	R	800
11	31/01	10	10:45	11:26	41	P	600
12	31/01	10	11:32	12:09	37	P	200
13	01/02	10	14:30	15:33	63	A	650
14	01/02	12	14:13	15:16	63	A	700
15	02/02	12	09:36	10:25	49	A	750
16	04/02	10	15:35	16:37	62	R	950
17	04/02	12	12:48	14:07	79	A	900
18	04/02	12	15:35	16:58	83	A	960
19	05/02	10	08:06	09:08	62	A	900
20	05/02	10	10:16	11:20	64	A	850
21	05/02	12	10:17	11:17	61	R	1200
22	06/02	7	11:33	12:28	55	A	900
23	06/02	10	12:55	13:52	57	R	1000
24	06/02	10	14:45	15:42	57	A	900
25	06/02	10	15:57	16:43	46	A	900
26	07/02	7	10:01	10:52	51	R	940
27	07/02	10	10:00	10:55	55	R	850
28	07/02	10	12:07	13:16	69	R	970
29	08/02	7	09:30	10:43	73	A	1000
30	08/02	7	11:06	12:10	64	R	850
31	08/02	7	13:51	14:47	56	A	850
32	08/02	7	15:21	16:08	47	A	800
33	08/02	10	09:29	10:50	81	P	1200
34	08/02	10	11:07	12:04	57	P	1200
35	08/02	10	13:48	14:51	63	A	770
36	08/02	10	15:07	16:15	68	R	900
37	09/02	7	08:13	09:22	69	A	900
38	09/02	7	09:53	10:55	62	A	850
39	09/02	7	14:19	15:24	65	A	850
40	09/02	7	15:49	16:52	63	A	800
41	09/02	10	08:16	09:25	69	P	1300
42	09/02	10	09:53	10:52	59	R	950

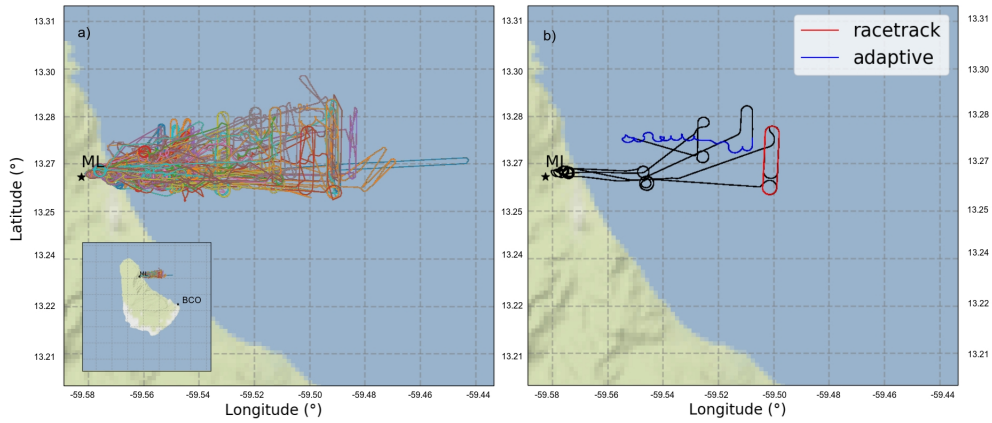

FIGURE 3 a) Trajectories of all SkyWalker-X6 RPAs during the NEPHELAE-EUREC^{4}A field campaign. The adaptive sampling and racetrack trajectories are represented in b). The black stars correspond to the Barbados Cloud Observatory (BCO) and Morgan Lewis (ML) location.

until arbitrarily transecting a cloud. Once a cloud had been identified, the autonomous cloud tracking strategy was implemented. The average wind during in the campaign is about 6 ± 2.4 m s^{-1} from the west north west generating a racetrack somewhat parallel to the coast (Fig. 3).

The first twelve flights were used to validate the payload instruments. The adaptive flights began on 1 February.

2.2.1 | Racetrack patterns

The 19 flights operated in a racetrack patterns between 2 and 3 km long and perpendicular to the prevailing wind to sample as many individual clouds as possible. These flights are used to produce a statistical overview of the cloud structure, characterizing the cloud core and the cloud shell similar to previous studies (Mallaun et al. (2018)). Based on the airspeed of the RPA (around 15 m s^{-1}), it takes about 30 s to transect a cloud with a 500 m dimension.

2.2.2 | Adaptive exploration

In this study, an adaptive sampling strategy was successfully implemented using RPAs to follow cumulus clouds and to retrieve a cloud heterogeneities, building on earlier studies by Verdu et al. (2020) and Maury et al. (2022)

During the field campaign, the adaptive sampling trajectory named 'Trinity' (Verdu et al. (2019)), was used to measure the cloud and environment variables. Once the cloud edge is detected by the CS, the RPA starts a turn inside the cloud to exit the cloud along a circular arc (radius ca. 120 m) and then re-enter the cloud while the autopilot adjusts the relative cloud position using a prescribed advective wind. The 'Trinity' pattern was preferred to the 'Rosette' pattern in Maury et al. (2022) since the clouds sampled during the field campaign were relatively small. The adaptive exploration started when an intercepted cloud along the initial racetrack had a transect length at least 100 m and a LWC$_{CS}$ greater than 0.01 g m^{-3}.

3 | RESULTS

3.1 | Thermodynamic variable comparison

The RPA profiles were compared to the radiosoundings carried out at the BCO every four hours (Albright et al. (2020)) during the NEPHELAE-EUREC^{4}A campaign. The difference between potential temperature and water vapour content up to 1000 m asl measured by the RPA and the closest radiosounding before the flight was calculated and is shown in Fig. 4.

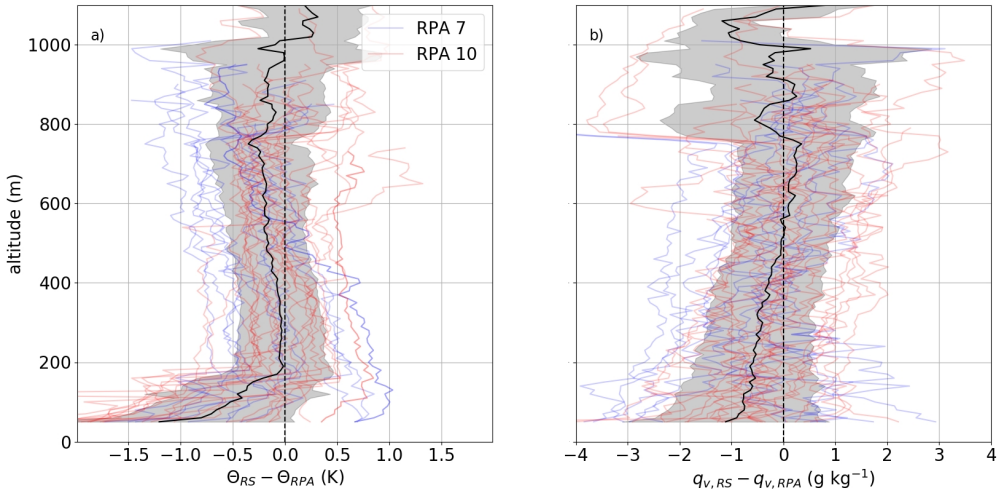

FIGURE 4 Difference between vertical profile of a) potential temperature and b) vapour content derived by BCO radiosoundings and RPA profiles. Blue lines correspond to RPA 7 and red line for RPA 10.

A systematic offset between the RPA and radiosounding up to 2 K is observed, probably related to instrument calibration. Systematic offsets have been adjusted post-campaign using the radiosounding as the reference.

The profiles of q_v of RPA 7 and 10 in the lower part of the boundary layer (< 200 m asl), systematically diverge from the radiosounding profile and probably related to terrestrial surface heating. The take-off was always into the wind towards the ocean; then the RPA began a holding pattern over the operations above the Morgan Lewis field area at 200 m asl (Hattenberger et al. (2022)). Consequently, the RPA meteorological measurements are biased by the terrestrial heat flux, particularly near the surface.

Above 200 m asl, the mean $\Delta\theta$ (black line in Fig. 4,a) is close to 0, with a tendency to become negative with altitude. A standard deviation of $\pm$ 0.5 K account for the variability in θ over all of the flights. There is also variability in these comparisons because some of the radiosoundings have been launched several hours before the RPA flight. For Δq_t, the trend becomes positive with altitude while remaining close to zero (Fig. 4,b). Above 800 m asl, the RPA often transected clouds, which generated additional variability in comparing with the radiosonde profiles. We also compared RPA profiles with the nearest radiosounding after the flight (not shown), and resulted in similar analysis, with an insignificant change in $\Delta\theta$ and Δq_t. These results confirm regional-scale homogeneity of meteorological conditions in the marine boundary

layer.

3.2 | Cloud statistics sampled from racetracks

In this section, only racetrack flights without adaptive sampling are presented. All flights took place in the cloud layer, between 50 and 250 meters above cloud base (m acb). To facilitate the comparison between flights, the altitude of the RPAs is expressed as a height m acb where the cloud base is estimated with the BCO ceilometer.

The results in this section characterize the horizontal structures of the clouds at a given altitude. Also, to facilitate the interpretation of the results, only the legs perpendicular to the advective wind are used. The turns at each end of the racetracks are excluded from the analysis.

3.2.1 | Cloud transects - statistical analysis

This section presents a statistical analysis of cloud transects for a single flight on 4 February (Flight 16) while the RPA followed a racetrack pattern. The cloud transects are presented in Fig 5. The altitude for this flight is 950 m asl, which is 250 m acb. The RPA observes altitude fluctuations of $\pm$ 10 m, generally resulting either from the turns at each end of the racetrack or from the ascending/descending air currents.

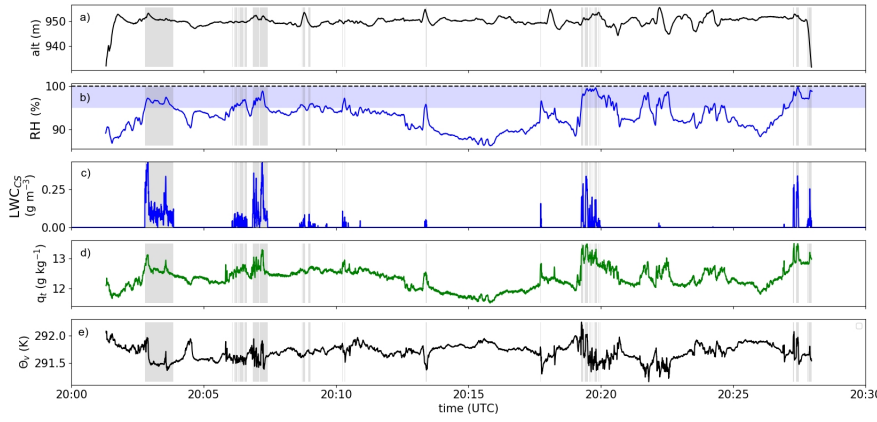

FIGURE 5 Time series of the racetrack pattern for flight 16 (4 February) a) flight altitude, b) relative humidity, c) total water content, d) virtual potential temperature and e) LWC$_{CS}$. The blue shaded area corresponds to a relative humidity $\geq$ 95%. The grey shaded areas correspond to the presence of a cloud.

The peaks of LWC$_{CS}$ correspond to RPA passages through a cumulus cloud with q_t values up to 14 g kg^{-1} and changes in θ_v up to 0.25 K greater than cloud-free air. We define a cloud when the following criteria are fulfilled: a relative humidity greater than 95% and a LWC$_{CS}$ greater than 0.01 g m^{-3} for at least 100 m (six seconds).
The presence of cloud is indicated by the grey shaded areas in Fig 5. During the racetrack pattern, 12 cumulus clouds were transected, each with different transect lengths and thermodynamic values. To study the cumulus cloud and its interactions with the environment that surrounds it, the meteorological state (T, RH) is characterized before intercepting the cloud, during the transect, as well as after exiting the cloud. Each transect is normalized to a length ranging from -0.5

to 0.5, with an environment around the cloud normalized from -1 to -0.5 and 0.5 to 1 (Fig. 6) to analyze the structure of the cloud and its surrounding environment. The environment before cloud entry is always described between -1 and -0.5 and the environment after cloud exit between 0.5 and 1. The normalized spatial resolution in Fig. 6 is 0.05, allowing up to 20 points to represent the cloud transect and surrounding environment. In-situ measurements are averaged to the length scale of the normalized transect.

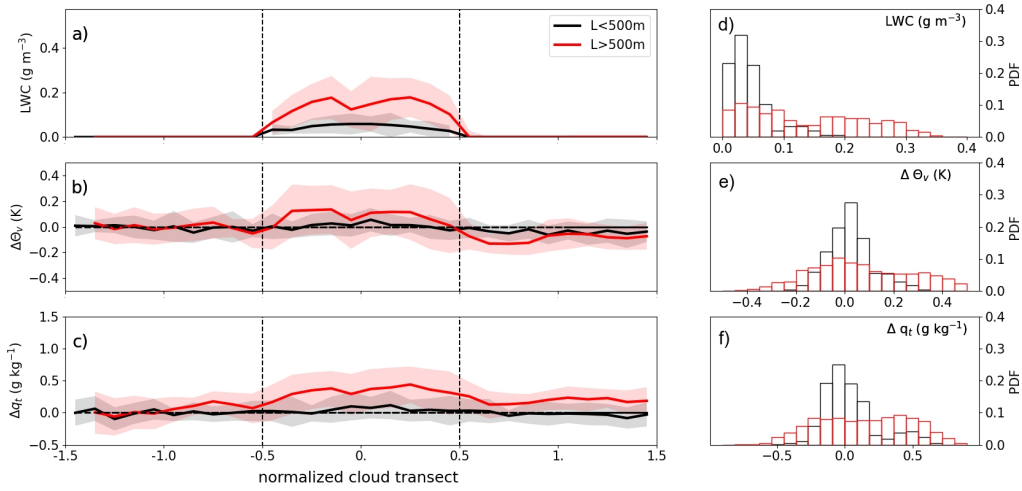

FIGURE 6 Normalized horizontal transects of a) LWC$_{CS}$, b) $\Delta\Theta_v$ and c) Δ q$_t$ and their standard deviation (shaded area) for clouds with a transect length smaller (larger) than 500 m represented by black lines (red lines) during the racetrack flights. The normalized cloud transect length corresponds to the distance between -0.5 and 0.5 and the environment before the cloud entry normalized to -1.5 and 0.5 (0.5 and 1.5 after the cloud exit). The PDF of each variable in d),e),f) are plotted on the right for both types of cumulus clouds.

Based on the time series of LWC$_{CS}$, the cloud observations have been statistically divided into two cloud populations: transects with lengths smaller than 500 m (corresponding to black lines in Fig. 6) and those with lengths greater than 500 m (corresponding to red lines in Fig. 6). This size criterion has been determined by two clusters with a K-means method, linking the transect lengths of the clouds either to the maximum buoyancy or to the maximum value of LWC. Note that transect length smaller than 500 m does not necessarily mean that the smallest dimension of the cumulus cloud is less than 500 m, as the trajectories do not necessarily pass through the cloud's center and clouds are of irregular shape.

The clouds with transects less than 500 m are characterized by low $\overline{LWC_{CS}}$, 0.11 $\pm$ 0.03 g m^{-3} and a negative/neutral buoyancy. This negative/neutral buoyancy can be either the consequence of a forced cloud (updraft driven and within a few 10 s of meters from the cloud base but not having released enough heat by condensation to be more buoyant than its environment), or a dissipating cloud. On average, the small clouds show a q_t difference between cloud core and environment close to 0, indicating that most of them are dissipating. These cloud states are confirmed by a conservative variable, liquid potential temperature, Θ_l, which is weaker in small clouds than the environment (not shown).

Clouds associated with transects larger than 500 m have a LWC$_{CS}$ average of 0.18 $\pm$ 0.07 g m^{-3} within the cloud core (and within 250 m of cloud base) and are composed by a buoyant cloud core (Θ_v core > Θ_v environment). As shown in Fig 6,b, a negatively buoyant shell is visible on the edge of the cloud and extends into the surrounding environment. The difference of θ_v between the cloud and the environment provides insight on the cloud buoyancy and entrainment mixing.

In Fig 6,c, we have plotted the deviation of the conservative variable, q_t of the cumulus clouds compared to the environment. An increase of q$_t$ in the cloud core of 0.2 $\pm$ 0.15 g kg^{-1} is observed for large clouds, which is consistent with a thermal transporting warm and moist air from below the cloud base. As mentioned previously, the q_t difference between cloud core and its environment is close to 0 for small clouds (< 500 m transect length).

Individual transects show a large variability around this mean (Fig. 6,d,e,f). The clouds associated with high LWC$_{CS}$ values also have high positive buoyancy at the core and negative buoyancy in their shell (not shown). No measurement inside the cloud core region attains the theoretical value of the adiabatic LWC, estimated to be 0.5 $\pm$ 0.1 g m^{-3}. The adiabatic LWC$_{CS}$ based on Korolev (1993) (2 g m^{-3} km^{-1}) is estimated using the altitude above cloud base (250 m) and the $\pm$ 50 m variability associated with cloud base height as measured by the ceilometer. The in-situ cloud observations point to a sub-adiabatic cloud parcel as also reported in previous observations of small cumuli (Rauber et al. (2007), Roberts et al. (2008), Sanchez et al. (2017)). The LWC$_{CS}$ for all clouds in this study remains relatively constant within the cloud core, and is consistent with other research aircraft observations (Roberts et al. (2008), Katzwinkel et al. (2014)).

To study the region inside and surrounding the cloud, we represent a thermodynamic diagram relating the buoyancy to the difference between q_t and $q_{t,sat}$ (Eq. 3). Zhao and Austin (2005a) used similar thermodynamic diagrams from outputs of a LES simulation of a non-precipitating oceanic cumulus case and identified four zones that correspond to $i_/$ saturated positively buoyant air (SP), $ii_/$ saturated negatively buoyant air (SN), $iii_/$ unsaturated positively buoyant air (UP), and $iv_/$ unsaturated negatively buoyant air (UN). SP and SN are saturated conditions corresponding to the cloud core and cloud edge, respectively; while UP and UN correspond to the unsaturated air surrounding the cloud. The shape of the V-graph obtained with the RPA observations for the 12 independent transects for this case study is similar to reported in Zhao and Austin (2005a).

Some clouds (e.g., 6,7, and 11 in Fig. 7) correspond to cases with transects larger than 500 m are located on the line of neutral buoyancy ($\Delta\Theta_v$=0) and a maximum of q_t. They are all made of a buoyant core (SP zone) and a non-buoyant edge (SN zone). These cores are associated with relatively high values of LWC$_{CS}$ as shown in Fig. 7,b. While Cloud 10 has a transect length less than 500 m, this cloud seems to be in full development phase and also has a buoyant core. On the contrary, clouds with transects less than 500 m (e.g., Clouds 3, 8, 9, 13) are composed only of neutrally buoyant air mass with a negatively buoyant shell (UN-SN zone). They are probably forced clouds, following the definition in Mallaun et al. (2019), with a LWC$_{CS}$ around 0.1 g m^{-3}. Clouds 1, 2, 4, 5 and 12 seem to be dissipating as they have a neutral or negative buoyancy with a q_t lower than $q_{t,sat}$, yet elevated LWC$_{CS}$ values around 0.2 g m^{-3}.

3.2.2 | Thermodynamic properties of trade-wind cumulus

Expanding on the case study from the previous section, all flights that were conducted by the racetracks are exploited here to generalize the relationship between cloud size and thermodynamic properties. The RPA flights were conducted at three altitudes above cloud base (50, 150 and 250 m), and a total of 39 clouds were sampled by racetrack patterns during the field campaign. This analysis describes the relationship between LWC, buoyancy and q_t for different heights above cloud base.

All clouds intercepted during the racetracks are shown in Fig. 8, and all measurements, cloudy or not, are shown in

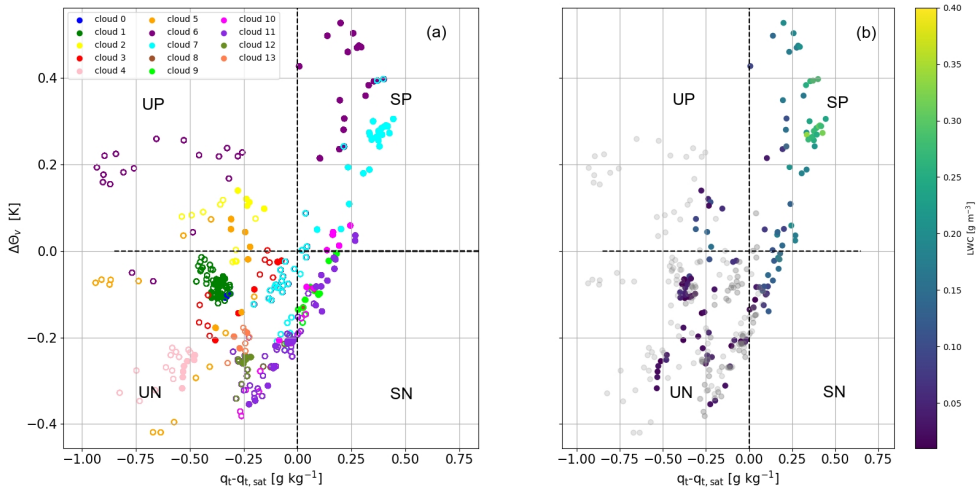

FIGURE 7 Thermodynamic diagram ($\Delta\Theta_v$ versus $q_t - q_{t,sat}$) for clouds sampled during the racetrack pattern of flight 16. a) Solid markers correspond to LWC$_{CS}$ > 0.01 g m^{-3} and empty marker correspond to surrounding environmental air. b) The LWC$_{CS}$ determined from the Cloud Sensor is represented with color and environmental air is represented in grey. The quadrants are designated by SP, saturated positive buoyancy; SN, saturated negative buoyancy; UP, unsaturated positive buoyancy; UN, unsaturated negative buoyancy.

the thermodynamic diagram. The expected V-shape is visible, and in-cloud measurements are generally located in the oversaturated zone (S; q_t-$q_{t,sat}$ > 0) with a majority of measurements in the SN zone (non-buoyant). The measurement uncertainty associated with $q_{t,sat}$ is estimated to be $\pm$ 0.19 g kg^{-1}, which may partly explain the presence of non-cloudy measurements in saturated areas. Forced and active clouds can be distinguished in Fig. 8. Forced clouds reside exclusively in the SN area (flight 16) while active clouds reside in the SN and SP areas and show a linear trend between the two areas. Most of the forced clouds correspond to transects at 50 m and 150 m acb, while the active clouds were sampled between 150 and 250 m acb.

While cloud transects provide a snapshot of the thermodynamic properties of the clouds, a statistical analysis of many individual clouds is required to study the cloud's life cycle (i.e., growth, mature and dissipation phases). The following section explores a new strategy for studying the cloud's life cycle.

3.3 | Temporal evolution of trade-wind cumulus

This section focuses on measurements obtained when following the spatio-temporal evolution of individual cumulus cloud using sensor-based navigation. The mission always starts with a racetrack pattern perpendicular to the wind direction at a given altitude above cloud base. Once a cloud has been identified, the adaptive sampling strategy is initiated using the CS and PTU sensors (Section 2.2.2). The adaptive sampling then continues autonomously using a pre-defined strategy until the cloud dissipates (Verdu et al. (2019),Maury et al. (2022)) or until the adaptive sampling has been terminated by an operator.

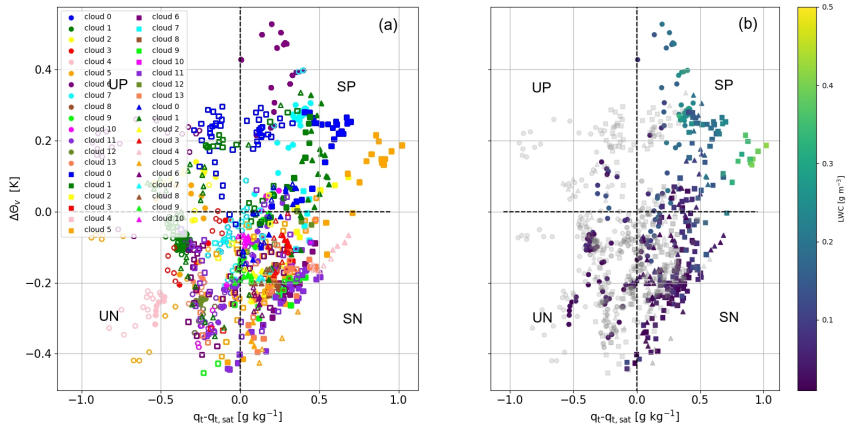

FIGURE 8 Same as Fig. 7 for clouds sampled during the racetrack pattern for flights 16 (circle), 23 (square) and 27 (triangle).

3.3.1 | Adaptive sampling by a single RPA

Case study - Flight 29

In flight 29 (Table 1), the RPA autonomously followed a cloud for almost eight minutes, conducting 12 transects at 150 m acb (1000 m asl) as shown in Fig. 9,a. During this exploration, the cloud evolved and the different phases of its life cycle were identified using thermodynamic diagrams (as in Section 3.2.1). The RPA conducted 15 transects of the cloud during the eight minutes of adaptive sampling, which corresponds to a transect approximately every 30 seconds. The first phase identified as the development phase (Fig. 9,c), corresponds to the beginning of the exploration until reaching the maximum LWC$_{CS}$ (0.27 g m^{-3},14:07). At 150 m acb, the adiabatic limit is 0.3 g m^{-3} which provides an upper limit for expected measurements of LWC.

During the development phase, the in-situ measurements also identify the shell with negative buoyancy and a cloud core associated with positive buoyancy. The measurements made by the RPA converge towards the saturated and positively floating values (i.e., SP zone) during this development phase (Fig. 9,c).

The mature phase (Fig. 9,d) is defined from approximately the time of LWC$_{CS}$ maximum to the time of buoyancy maximum. In the mature phase, the LWC$_{CS}$ values in the cloud core (i.e., SP zone) become more variable with a maximum LWC$_{CS}$ approaching 0.25 g m^{-3}. During the mature phase, few measurements were located in the UP zone (non-cloudy air), because the Trinity pattern (Verdu et al. (2020)) initiates a circular arc after the RPA exits the cloud and the RPA remains in close proximity to the cloud (< 100 m horizontal distance).

The dissipation phase (Fig. 9,e),comprises the period from the buoyancy maximum until the RPA can no longer follow the cloud. In the dissipation phase, the measurements are all significantly non-buoyant and some q_t anomalies remain above 0.1 g kg^{-1}, while the LWC$_{CS}$ measurements decrease to 0.1 g m^{-3}. These results suggest that the cloud is diluting.

During the mature and dissipation phases, the measurements converge towards negative buoyancy in both the cloud (SN zone) and in envelope surrounding around the cloud (UN zone) as shown in Fig. 9,b.

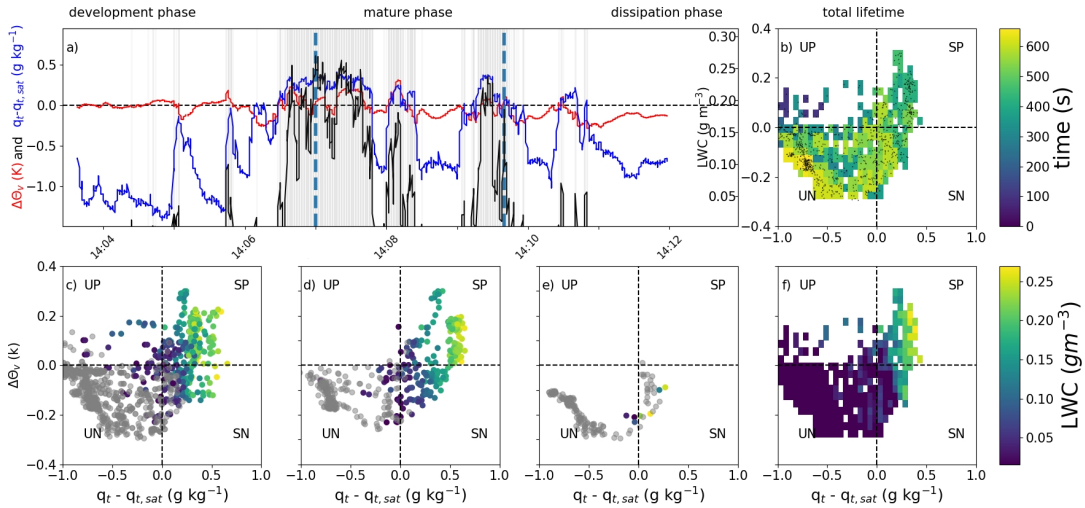

FIGURE 9 a) Time series of $\Delta\Theta_v$, q_t-$q_{t,sat}$ and LWC$_{CS}$ during the adaptive sampling for the Flight 29. The three cloud phases of the cumulus cloud are represented, separated by a vertical dashed blue lines. The shaded grey area corresponds to cloud presence (LWC$_{CS}$ > 0.01 g m^{-3}) and the horizontal dashed line corresponds to a saturated environment ($q_{t,sat}$). The thermodynamic diagram for the entire time series as a function of time (b) and LWC$_{CS}$ (f) with black points representing the in-situ measurements. The thermodynamic diagram for each cloud phase identified during the adaptive exploration as a function of LWC$_{CS}$ is shown in c) development phase, d) mature phase, e) dissipating phase. The non-cloudy environmental air is represented by the grey markers. UP, UN, SN, SP represent the unsaturated positive buoyant zone, unsaturated negative buoyant zone, saturated negative buoyant zone and saturated positive buoyant zone, respectively.

Overview of autonomous adaptive sampling of clouds

During the campaign, 18 adaptive sampling flights were performed (noted as A in Table 1). Four adaptive sampling flights exceed eight minutes of tracking the cloud, namely for flights 19, 22, 38 and 39. The in-situ measurements of the tracked clouds are shown in the thermodynamic diagram in Fig. 10 and all exhibit the expected V-shape. The highest LWC$_{CS}$ values are concentrated in the supersaturated and buoyant zone (SP zone) during flights 19 and 39. For the cloud followed during flight 22, the buoyancy values are negative throughout the cloud, which is likely related to sampling 70 m acb – a zone close enough to cloud base that is generally not buoyant because it is still forced by the thermals below the cloud. The thermodynamic diagrams show that all adaptively sampled clouds trend towards non-buoyant and q_t (and LWC) decrease as a function of time, which suggests that cloud tracking began after or near the end of the development phase. The reduction in q_t is related to entrainment mixing between the moist cloudy air and the environment.

Clearly, a single transect is insufficient to observe the change of a conservative variable during the cloud's life cycle. The adaptive sampling strategy highlights the potential of RPA for studying clouds (and other atmospheric phenomena) semi-continuously to observe the spatial and temporal evolution.

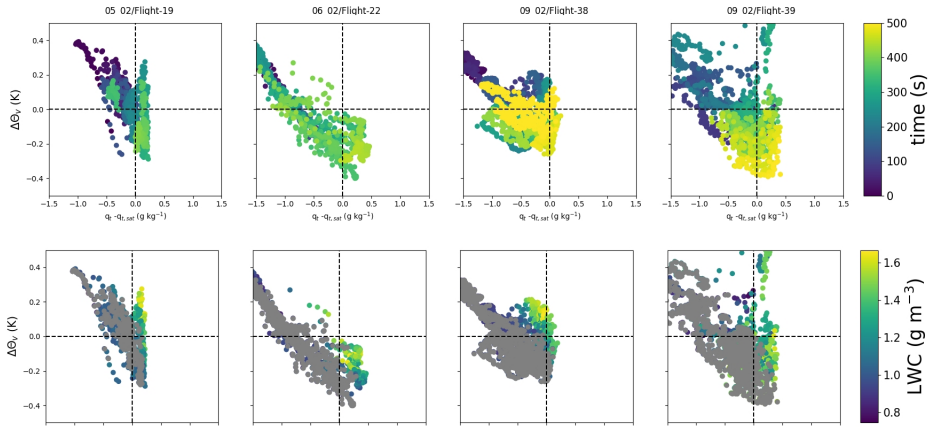

FIGURE 10 Thermodynamic diagram ($\Delta\Theta_v$ versus $q_t - q_{t,sat}$) for clouds sampled by adaptive exploration for flights 19 (first column), 22 (second column), 38 (third column) and 39 (fourth column). The first row represents the time after the beginning of exploration and the second row represents the LWC_{CS}. The environmental air measurements are represented in grey.

3.3.2 | Adaptive sampling with two RPAs

Temporal and vertical evolution of thermodynamic variables

In the previous section, we demonstrate the capabilities of sensor-based adaptive sampling to observe a dynamic atmospheric process such as following the temporal evolution of a cloud. In this section, we extend these capabilities by deploying two RPAs at different altitudes simultaneously to follow the same cloud. In this section, two RPAs (RPA_{70} and RPA_{150}) flew at the same time (flight 35 and 31) at two different altitudes, 770 m asl and 850 m asl, corresponding to 70 m and 150 m acb, respectively. The cloud base, determined by the ceilometer located at BCO, was at 700 m. At 18:31 UTC (14:31 LT), RPA_{70} detects a cloud and the adaptive sampling is initiated. The information is subsequently sent to the second RPA (RPA_{150}) to go to the same GPS position and 80 m higher, which takes about two minutes. Simultaneous adaptive sampling by both RPAs continues for seven minutes at two altitudes - each RPA conducts its adaptive sampling independently.

RPA_{150} and RPA_{70} conducted 14 and 15 transects through the cumulus cloud, respectively. As the RPAs did not make entries in the cloud at the same time, the comparison between the two samples was made by the closest transect and within the same minute. Eight transects for each RPA can be compared with a duration varying from 5 to 50 seconds and are represented in the Fig. 14.

The values of the difference between the median q_t in the cloud and its environment are plotted in Fig. 11,a for both RPAs (red for RPA_{70} and blue for RPA_{150}) and for each transect. As expected, q_t is higher than the environment at both levels, but this difference is more pronounced for RPA_{70} (0.8 ± 0.2 g kg^{-1}) than RPA_{150} (0.16 ± 0.14 g kg^{-1}).

This evolution of the conservative variable, q_t, shows mixing processes which have impacted the cumulus cloud. To quantify the mixing, we use the mass fraction of adiabatic cloudy air, χ, defined in Eq.7. It varies between 0.2 and 0.54 with a median value around 0.36, meaning that more than half of the air in the cloud has been entrained, leading to the dilution of the cloud. These results are similar to previous studies, as Sanchez et al. (2021) for stratocumulus clouds in

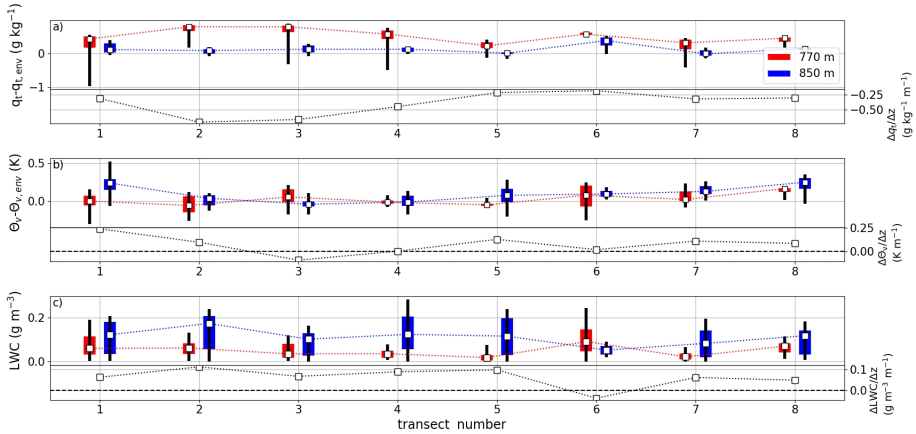

FIGURE 11 Median values (white points), 25th-75th percentile values (color bars) and min/max values (black vertical lines) for q_t in a), Θ_v in b) and LWC$_{CS}$ in c) for RPA$_{150}$ (blue color) and RPA$_{70}$ (red color) during the eight nearly simultaneous transects for adaptive exploration of two RPAs (flights 31 and 35). The vertical gradients of each median variable for each corresponding transect pair are represented in black.

the Southern Ocean (χ between 0.28 and 0.56).

Expanding on the previous sections, the thermodynamic diagrams of the tracked cloud are reproduced at 70 and 150 m acb summarizing the adaptive exploration as shown in Fig. 12.

For both altitudes, the saturated vapour content, $q_{t,sat}$, is computed by averaging the non-cloudy air temperature prior to the adaptive exploration to avoid being biased by the cloud shell and in-cloud measurements. We assume that $q_{t,sat}$ is therefore constant at a given altitude in the region surrounding the cloud and is advected uniformly as the cumulus cloud evolves. $q_{t,sat}$ is 10.35 $\pm$ 0.04 g kg^{-1} at 70 m acb and 10.24 $\pm$ 0.04 g kg^{-1} at 150 m acb (dotted vertical line on Fig. 12). The average of θ_v in the environment surrounding the cloud, used to compute buoyancy (Eq.6), is computed the same way. As in Section 3.1, the four zones (SP, SN, UP, UN) are defined and the temporal evolution of the cloud is documented.

For the observations at 70 m acb (Fig. 12), LWC$_{CS}$ remains low as expected, and the V-shape is less pronounced than for observations at 150 m acb. At 150 m acb (Fig. 12), the dispersion of thermodynamic variables is larger in the cloud: the difference of θ_v with the environment can reach 0.36 K at the maximum in the cloud core (compared to 0.25 K at 70 m acb).

As the sampling progresses, observations at both altitudes show a convergence towards neutral buoyancy for both the cloud and its surrounding environment – indicative of mixing and dissipation of the cloud. During the first 200 seconds of adaptive sampling, most in-cloud measurements exhibit a positively buoyant core (SP and SN quadrants) with a shell around the cloud that is developing. As the cloud transects continue, the cloud and the surrounding environment become exclusively negatively-buoyant, and always associated with a relatively high q_t that is converging to $q_{t,sat}$. Once the air parcels reach $q_{t,sat}$, the cloud has nearly dissipated at this altitude (particularly at 70 m above the initial cloud base) and there is no difference between the shell, the rest of the cloud, and the surrounding environment.

The thermodynamic variables (θ_v, q_t) at 150 m acb also evolve temporally towards to a neutrally buoyant environ-

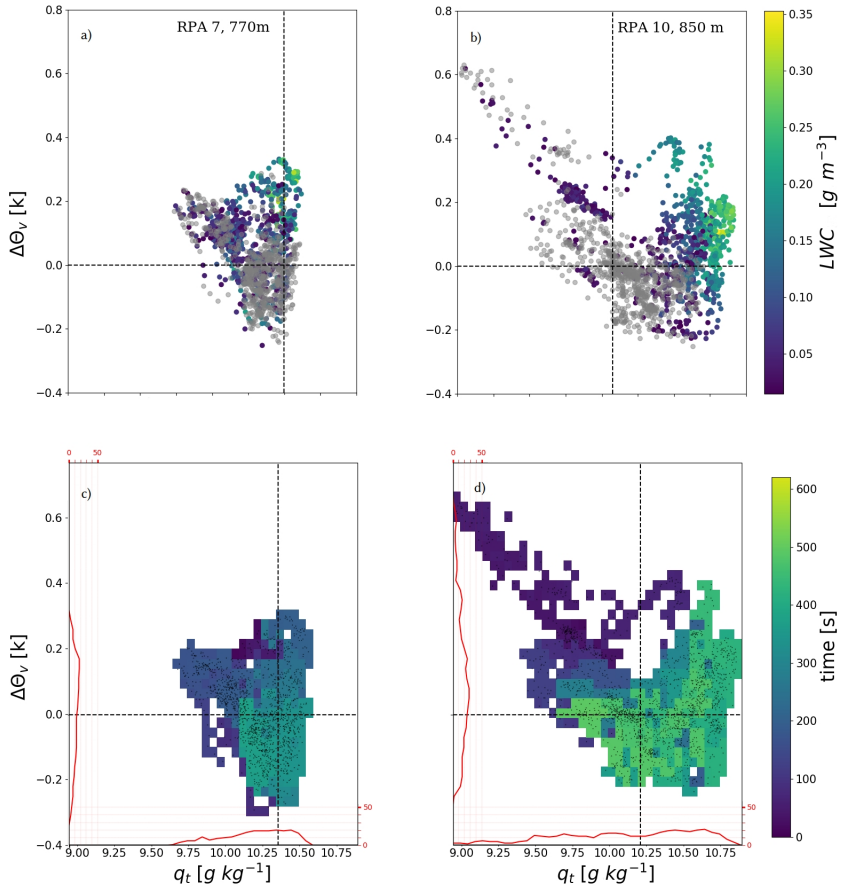

FIGURE 12 Thermodynamic diagram showing the relationship between virtual potential temperature, Θ_v, and total water, q_t. The colorbar represents LWC_{CS} (a,b) and time (c, d) for 70 m acb (a, c) and 150 m acb (b, d). The horizontal dotted black line represents the mean Θ_v of the environment and vertical dotted black line represents the the saturated water content ($q_{t,sat}$). The black points represent the in-situ meaurements and grey points represent the non-cloudy environmental air. The red lines represent the in-situ measurements used to determine the value of Θ_v and q_t.

ment. However, at the end of the exploration, there are still buoyant parts in the cloud at 150 m acb, which means that the cloud has not completely dissipated. The rising of the cloud base has also been visually verified by the onboard cameras.

Thermodynamic diagrams: observations versus simulations

In Maury et al. (2022), high resolution LES trade wind cumuli were studied and used as an exploration field for virtual adaptive sampling at 150 m acb – similar to the in-situ measurements in this study. The thermodynamic diagram from the numerical simulations corresponding to the cloud N2 in Maury et al. (2022) representing its entire life cycle is shown

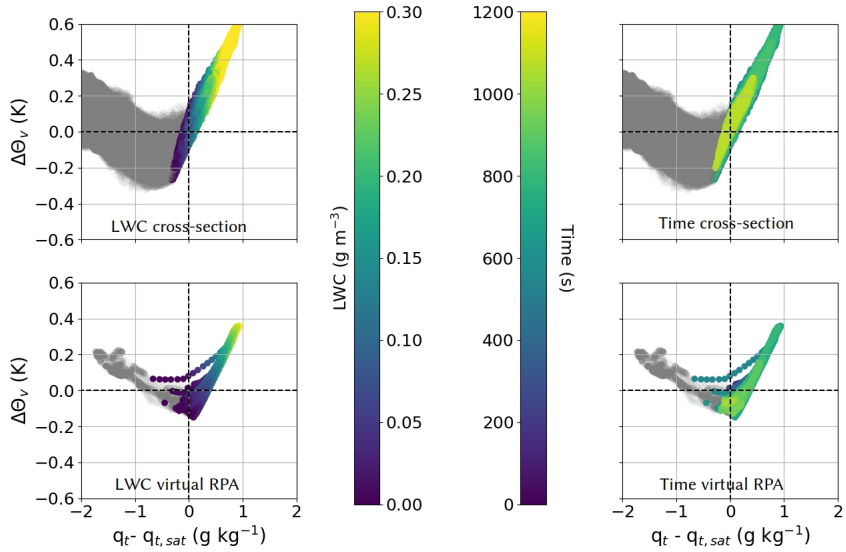

FIGURE 13 Thermodynamic diagram ($\Delta\Theta_v$ versus $q_t - q_{t,sat}$) for a cross section of a simulated cloud (first row) and virtually sampled by adaptive RPA exploration (second row) at 150 m acb. The colors represent the LWC$_{CS}$ values (first row) and time after the appearance of the simulated cloud and grey points represent environmental air. Simulations based on cloud N2 described in Maury et al. (2022)

in Fig. 13. Figure 13,a shows the thermodynamic diagram for the cross section at 150 m acb, while Fig. 13,b illustrates the thermodynamic diagram as observed by a virtual RPA after adaptive sampling. The results using the LES (Fig. 13,a and Fig. 13,b) reproduces the cumulus V-shape with high LWC$_{CS}$ associated with high buoyancy, θ_v, and total water, q_t. The simulated buoyancy and LWC$_{CS}$ values approach the adiabatic limit, while the in-situ observations from the RPA are significantly less (0.38 K and 0.25 g m^{-3} for the observations versus 0.6 K and 0.3 g m^{-3} for the LES simulation). Observations and simulations both show the convergence toward neutrally buoyant air as a function of time..

The dispersion is greater in the RPA observations compared to the numerical simulations in part because of uncertainty associated with the derivation of $q_{t,sat}$ ($\pm$ 0.19 g kg^{-1} from Section 3.2) and θ_v ($\pm$ 0.05 K). Nonetheless, results suggest that the LES produce less heterogeneities than observed in real cumulus clouds, reflecting the parameterization of fine-scale turbulence leading to an underestimation of entrainment in cloud. The turbulence parameterization from Cuxart et al. (2000) is used in the simulations in Maury et al. (2022). Another factor may be the one-moment bulk microphysics scheme used (ICE3 scheme; Pinty and Jabouille (1998)), which assumes a constant number of cloud droplets (set at 300 cm^{-3}). Instead of a one-moment scheme, the use of a two-moment scheme has been shown to introduce more heterogeneities in cloud microphysical properties in simulated cumuli (Brenguier and Grabowski (1993),Chandrakar et al. (2021)).

Another difference is cloud cores from the RPA observations are sub-adiabatic, which is not reflected adiabatic cloud cores simulated in Maury et al. (2022). These results suggest that the time scales of mixing in LES are insufficient to reproduce inhomogeneous mixing observed in small cumuli (Sanchez et al. (2020), Beals et al. (2015)).

4 | CONCLUSION

The study presented here summarizes the Remotely Piloted Aircraft (RPA) observations of trade-wind cumulus clouds in the tropical western Atlantic Ocean during the NEPHELAE-EUREC^{4}A field campaign. During the campaign, more than 40 trade wind cumuli were transected by lightweight RPA instrumented with meteorological and cloud sensors to characterize their thermodynamic state relating saturated / unsaturated and buoyant / non-buoyant parks of the clouds and its surroundings. The transects distinguished the difference between forced and actively convective clouds based on their size and thermodynamic properties. Using a K-means cluster analysis, clouds with transect lengths greater than 500 m have significantly higher Liquid Water Content (LWC) associated with their cores and positive buoyancy anomalies compared to smaller clouds. The comparison of the temperature and humidity data from the RPAs with those from the radiosoundings suggests regional scale homogeneity of meteorological conditions in the marine boundary layer.

For the first time, we also demonstrate the potential of sensor-based adaptive sampling to follow the evolution of an individual cloud throughout its lifetime. The RPA followed individual clouds for up to eight minutes transecting the cloud on average every 30 seconds. The duration of the adaptive sampling was mostly limited by dissipation of the cloud. The temporal evolution of conservative variable (total water content, q_t) and virtual potential temperature, θ_v, converge towards a stable saturated environment (q_t approaches $q_{t,sat}$) and a neutrally stable environment (buoyancy approaches zero), thus forming an expected V-shaped thermodynamic diagram. Adaptive sampling with two RPAs at 70 m and 150 m acb simultaneously characterized the thermodynamic and cloud microphysical properties. The V-shaped thermodynamic diagram is more pronounced at 150 meters above cloud base (m acb) compared to 70 m acb, owing to a more developed cloud with higher buoyancy and cloud water higher above cloud base. The observations at 70 m acb converge more rapidly towards neutral buoyancy and saturated conditions as the lower part of the cloud dissipates.

The in-situ observations have been also compared to high-resolution Large-Eddy Simulations (LES) and show similar shapes of thermodynamic diagrams. The simulations show less variability in the conservative variable q_t and θ_v and tend to overpredict the buoyancy and LWC in the cloud core, which is likely because the LES underestimate the scales of entrainment mixing.

CONFLICT OF INTEREST

The authors declare that they have no conflict of interest.

ACKNOWLEDGEMENTS

The NEPHELAE project to develop the RPA observing system used for this study was supported by Agence Nationale de la Recherche (Project-ANR-17-CE01-0003), Aerospace Valley and Météo-France. The authors acknowledge Bjorn Stevens, Sandrine Bony, David Farrell and all the scientific and technical researchers in the EUREC^{4}A project (financed by the European Research Council) for enabling this opportunity, the Caribbean Institute for Meteorology and Hydrology (CIMH) for radiosounding data and the Hoad family for letting us conduct the RPA operations on their land. The authors also thank Grégoire Cayez and Murat Bronz for their contributions in operating the RPA; and Fabrice Julien and Sophian Arixi for their contributions to preparing and operating the RPA and scientific payload.

REFERENCES

Albright, A. L., Fildier, B., Touzé-Peiffer, L., Pincus, R., Vial, J. and Muller, C. (2020) Atmospheric radiative profiles during eurec^{4}a. *Earth System Science Data Discussions*, **2020**, 1–17. URL: https://essd.copernicus.org/preprints/essd-2020-269/.

Barnes, G. M., Fankhauser, J. C. and Browning, W. D. (1996) Evolution of the vertical mass flux and diagnosed net lateral mixing in isolated convective clouds. *Monthly Weather Review*, **124**, 2764–2784.

Beals, M. J., Fugal, J. P., Shaw, R. A., Lu, J., Spuler, S. M. and Stith, J. L. (2015) Holographic measurements of inhomogeneous cloud mixing at the centimeter scale. *Science (New York, N.Y.)*, **350**, 87—90. URL: https://doi.org/10.1126/science.aab0751.

de Boer, G., Borenstein, S., Calmer, R., Cox, C., Rhodes, M., Choate, C., Hamilton, J., Osborn, J., Lawrence, D., Argrow, B. and Intrieri, J. (2022) Measurements from the university of colorado raaven uncrewed aircraft system during atomic. *Earth System Science Data*, **14**, 19–31.

Brenguier, J.-L. and Grabowski, W. W. (1993) Cumulus entrainment and cloud droplet spectra: A numerical model within a two-dimensional dynamical framework. *Journal of Atmospheric Sciences*, **50**, 120 – 136. URL: https://journals.ametsoc.org/view/journals/atsc/50/1/1520-0469_1993_050_0120_ceacds_2_0_co_2.xml.

Brown, A. R., Cederwall, R. T., Chlond, A., Duynkerke, P. G., Golaz, J.-C., Khairoutdinov, M., Lewellen, D. C., Lock, A. P., MacVean, M. K., Moeng, C.-H., Neggers, R. A. J., Siebesma, A. P. and Stevens, B. (2002) Large-eddy simulation of the diurnal cycle of shallow cumulus convection over land. *Quarterly Journal of the Royal Meteorological Society*, **128**, 1075–1093. URL: https://rmets.onlinelibrary.wiley.com/doi/abs/10.1256/003590002320373210.

Burnet, F. and Brenguier, J.-L. (2007) Observational study of the entrainment-mixing process in warm convective clouds. *Journal of the Atmospheric Sciences*, **64**, 1995–2011. URL: https://doi.org/10.1175/JAS3928.1.

— (2010) The onset of precipitation in warm cumulus clouds: An observational case-study. *Quarterly Journal of the Royal Meteorological Society*, **136**, 374–381. URL: https://rmets.onlinelibrary.wiley.com/doi/abs/10.1002/qj.552.

Calmer, R. (2018) *3D wind vectors measurement with remotely piloted aircraft system for aerosol-cloud interaction study*. Ph.D. thesis. URL: http://www.theses.fr/2018INPT0021. Thèse de doctorat dirigée par Roberts, Gregory Océan, atmosphère, climat Toulouse, INPT 2018.

Calmer, R., Roberts, G. C., Sanchez, K. J., Sciare, J., Sellegri, K., Picard, D., Vrekoussis, M. and Pikridas, M. (2019) Aerosol–cloud closure study on cloud optical properties using remotely piloted aircraft measurements during a bacchus field campaign in cyprus. *Atmospheric Chemistry and Physics*, **19**, 13989–14007. URL: https://acp.copernicus.org/articles/19/13989/2019/.

Chandrakar, K. K., Grabowski, W. W., Morrison, H. and Bryan, G. H. (2021) Impact of entrainment mixing and turbulent fluctuations on droplet size distributions in a cumulus cloud: An investigation using lagrangian microphysics with a subgrid-scale model. *Journal of the Atmospheric Sciences*, **78**, 2983 – 3005. URL: https://journals.ametsoc.org/view/journals/atsc/78/9/JAS-D-20-0281.1.xml.

Cuxart, J., Bougeault, P. and Redelsperger, J.-L. (2000) A turbulence scheme allowing for mesoscale and large-eddy simulations. *Quarterly Journal of the Royal Meteorological Society*, **126**, 1–30. URL: https://rmets.onlinelibrary.wiley.com/doi/abs/10.1002/qj.49712656202.

Gerber, H. E., Frick, G. M., Jensen, J. B. and Hudson, J. G. (2008) Entrainment, mixing, and microphysics in trade-wind cumulus. *Journal of the Meteorological Society of Japan. Ser. II*, **86A**, 87–106.

Hagen, M., Ewald, F., Groß, S., Oswald, L., Farrell, D. A., Forde, M., Gutleben, M., Heumos, J., Reimann, J., Tetoni, E., Köcher, G., Marinou, E., Kiemle, C., Li, Q., Chewitt-Lucas, R., Daley, A., Grant, D. and Hall, K. (2021) Deployment of the c-band radar poldirad on barbados during eurec^{4}a. *Earth System Science Data*, **13**, 5899–5914. URL: https://essd.copernicus.org/articles/13/5899/2021/.

Harrison, R. G. and Nicoll, K. A. (2014) Active optical detection of cloud from a balloon platform. *Rev. Sci. Instrum.*, **85**, 066104.

Hattenberger, G., Bronz, M. and Gorraz, M. (2014) Using the Paparazzi UAV System for Scientific Research. In *IMAV 2014, International Micro Air Vehicle Conference and Competition 2014*, pp 247–252. Delft, Netherlands. URL: https://hal-enac.archives-ouvertes.fr/hal-01059642.

Hattenberger, G., Verdu, T., Maury, N., Narvor, P., Couvreux, F., Bronz, M., Lacroix, S., Cayez, G. and Roberts, G. C. (2022) Field report: Deployment of a fleet of drones for cloud exploration. *International Journal of Micro Air Vehicles*, **14**, 175682932110708. URL: https://hal-enac.archives-ouvertes.fr/hal-03520657.

Heus, T. and Jonker, H. J. J. (2008) Subsiding shells around shallow cumulus clouds. *Journal of the Atmospheric Sciences*, **65**, 1003–1018. URL: https://doi.org/10.1175/2007JAS2322.1.

Hoffmann, F., Siebert, H., Schumacher, J., Riechelmann, T., Katzwinkel, J., Kumar, B., Götzfried, P. and Raasch, S. (2014) Entrainment and mixing at the interface of shallow cumulus clouds: Results from a combination of observations and simulations. **23**, 349–368.

Katzwinkel, J., Siebert, H., Heus, T. and Shaw, R. A. (2014) Measurements of turbulent mixing and subsiding shells in trade wind cumuli. *Journal of the Atmospheric Sciences*, **71**, 2810–2822. URL: https://doi.org/10.1175/JAS-D-13-0222.1.

Korolev, A. (1993) On the formation of non-adiabatic lwc profile in stratiform clouds. *Atmospheric Research*, **29**, 129 – 134. URL: http://www.sciencedirect.com/science/article/pii/016980959390041L.

Leriche, M. and Colomb, A. (2020) The BIO-MAÏDO (Bio-physicochemistry of tropical clouds at Maïdo (La Réunion Island): processes and impacts on secondary organic aerosols formation) campaign. In *EGU General Assembly Conference Abstracts*, EGU General Assembly Conference Abstracts, 19029.

Mallaun, C., Giez, A., Mayr, G. J. and Rotach, M. W. (2018) Subsiding shells and vertical mass flux in warm cumulus clouds over land. *Atmospheric Chemistry and Physics Discussions*, **2018**, 1–24. URL: https://www.atmos-chem-phys-discuss.net/acp-2018-825/.

— (2019) Subsiding shells and the distribution of up- and downdraughts in warm cumulus clouds over land. *Atmospheric Chemistry and Physics*, **19**, 9769–9786.

Maury, N., Roberts, G. C., Couvreux, F., Verdu, T., Narvor, P., Villefranque, N., Lacroix, S. and Hattenberger, G. (2022) Use of large-eddy simulations to design an adaptive sampling strategy to assess cumulus cloud heterogeneities by remotely piloted aircraft. *Atmospheric Measurement Techniques*, **15**, 335–352. URL: https://amt.copernicus.org/articles/15/335/2022/.

Neggers, R. A. J., Jonker, H. J. J. and Siebesma, A. P. (2003) Size statistics of cumulus cloud populations in large-eddy simulations. *Journal of the Atmospheric Sciences*, **60**, 1060–1074. URL: https://doi.org/10.1175/1520-0469(2003)60<1060:SSOCCP>2.0.CO;2.

Nicoll, K. A. and Harrison, R. G. (2012) Balloon-borne disposable radiometer for cloud detection. *Review of Scientific Instruments*, **83**, 025111. URL: https://doi.org/10.1063/1.3685252.

Pinty, J.-P. and Jabouille, P. (1998) A mixed-phase cloud parameterization for use in mesoscale non-hydrostatic model: simulations of a squall line and of orographic precipitations. In *Conf. on Cloud Physics*, 217–220. Amer. Meteor. Soc Everett, WA.

Rauber, R. M., Stevens, B., Ochs, H. T., Knight, C., Albrecht, B. A., Blyth, A. M., Fairall, C. W., Jensen, J. B., Lasher-Trapp, S. G., Mayol-Bracero, O. L., Vali, G., Anderson, J. R., Baker, B. A., Bandy, A. R., Burnet, E., Brenguier, J.-L., Brewer, W. A., Brown, P. R. A., Chuang, R., Cotton, W. R., Di Girolamo, L., Geerts, B., Gerber, H., Göke, S., Gomes, L., Heikes, B. G., Hudson, J. G., Kollias, P., Lawson, R. R., Krueger, S. K., Lenschow, D. H., Nuijens, L., O'Sullivan, D. W., Rilling, R. A., Rogers, D. C., Siebesma, A. P., Snodgrass, E., Stith, J. L., Thornton, D. C., Tucker, S., Twohy, C. H. and Zuidema, P. (2007) Rain in shallow cumulus over the ocean: The rico campaign. *Bulletin of the American Meteorological Society*, **88**, 1912–1928. URL: https://doi.org/10.1175/BAMS-88-12-1912.

Roberts, G. C., Ramana, M. V., Corrigan, C., Kim, D. and Ramanathan, V. (2008) Simultaneous observations of aerosol–cloud–albedo interactions with three stacked unmanned aerial vehicles. *Proceedings of the National Academy of Sciences of the United States of America*, **105**, 7370–7375. URL: http://doi.org/10.1073/pnas.0710308105.

Sanchez, K. J., Roberts, G. C., Calmer, R., Nicoll, K., Hashimshoni, E., Rosenfeld, D., Ovadnevaite, J., Preissler, J., Ceburnis, D., O'Dowd, C. and Russell, L. M. (2017) Top-down and bottom-up aerosol–cloud closure: towards understanding sources of uncertainty in deriving cloud shortwave radiative flux. *Atmospheric Chemistry and Physics*, **17**, 9797–9814. URL: https://www.atmos-chem-phys.net/17/9797/2017/.

Sanchez, K. J., Roberts, G. C., Diao, M. and Russell, L. M. (2020) Measured constraints on cloud top entrainment to reduce uncertainty of nonprecipitating stratocumulus shortwave radiative forcing in the southern ocean. *Geophysical Research Letters*, **47**, e2020GL090513.

Sanchez, K. J., Roberts, G. C., Saliba, G., Russell, L. M., Twohy, C., Reeves, J. M., Humphries, R. S., Keywood, M. D., Ward, J. P. and McRobert, I. M. (2021) Measurement report: Cloud processes and the transport of biological emissions affect southern ocean particle and cloud condensation nuclei concentrations. *Atmospheric Chemistry and Physics*, **21**, 3427–3446. URL: https://acp.copernicus.org/articles/21/3427/2021/.

Siebesma, A. P., Bretherton, C. S., Brown, A., Chlond, A., Cuxart, J., Duynkerke, P. G., Jiang, H., Khairoutdinov, M., Lewellen, D., Moeng, C.-H., Sanchez, E., Stevens, B. and Stevens, D. E. (2003) A large eddy simulation intercomparison study of shallow cumulus convection. *Journal of the Atmospheric Sciences*, **60**, 1201–1219. URL: https://journals.ametsoc.org/doi/abs/10.1175/1520-0469%282003%2960%3C1201%3AALESIS%3E2.0.CO%3B2.

Stevens, B., Bony, S., Brogniez, H., Hentgen, L., Hohenegger, C., Kiemle, C., L'Ecuyer, T. S., Naumann, A. K., Schulz, H., Siebesma, P. A., Vial, J., Winker, D. M. and Zuidema, P. (2020) Sugar, gravel, fish and flowers: Mesoscale cloud patterns in the trade winds. *Quarterly Journal of the Royal Meteorological Society*, **146**, 141–152. URL: https://rmets.onlinelibrary.wiley.com/doi/abs/10.1002/qj.3662.

Stevens, B. and Bony, S. e. a. (2021) Eurec^{4}a. *Earth System Science Data Discussions*, **2021**, 1–78. URL: https://essd.copernicus.org/preprints/essd-2021-18/.

Stevens, B., Lenschow, D. H., Vali, G., Gerber, H., Bandy, A., Blomquist, B., Brenguier, J.-L., Bretherton, C., Burnet, F., Campos, T. et al. (2003) Dynamics and chemistry of marine stratocumulus—dycoms-ii. *Bulletin of the American Meteorological Society*, **84**, 579–594.

Verdu, T., Hattenberger, G. and Lacroix, S. (2019) Flight patterns for clouds exploration with a fleet of UAVs. In *ICUAS 2019, 2019 International Conference on Unmanned Aircraft Systems*, Proceedings of International Conference on Unmanned Aircraft Systems (ICUAS), ISBN: 978–1–7281–0334–1. Atlanta, United States: IEEE.

Verdu, T., Maury, N., Narvor, P., Seguin, F., Roberts, G., Couvreux, F., Cayez, G., Bronz, M., Hattenberger, G. and Lacroix, S. (2020) Experimental flights of adaptive patterns for cloud exploration with UAVs. In *International Conference on Intelligent Robots and Systems (IROS 2020)*. Las Vegas (on line), United States. URL: https://hal.laas.fr/hal-02994385.

Zhang, Y., Klein, S. A., Fan, J., Chandra, A. S., Kollias, P., Xie, S. and Tang, S. (2017) Large-eddy simulation of shallow cumulus over land: A composite case based on arm long-term observations at its southern great plains site. *Journal of the Atmospheric Sciences*, **74**, 3229 – 3251. URL: https://journals.ametsoc.org/view/journals/atsc/74/10/jas-d-16-0317.1.xml.

Zhao, M. and Austin, P. H. (2005a) Life cycle of numerically simulated shallow cumulus clouds. part i: Transport. *Journal of the Atmospheric Sciences*, **62**, 1269–1290. URL: https://doi.org/10.1175/JAS3414.1.

APPENDIX

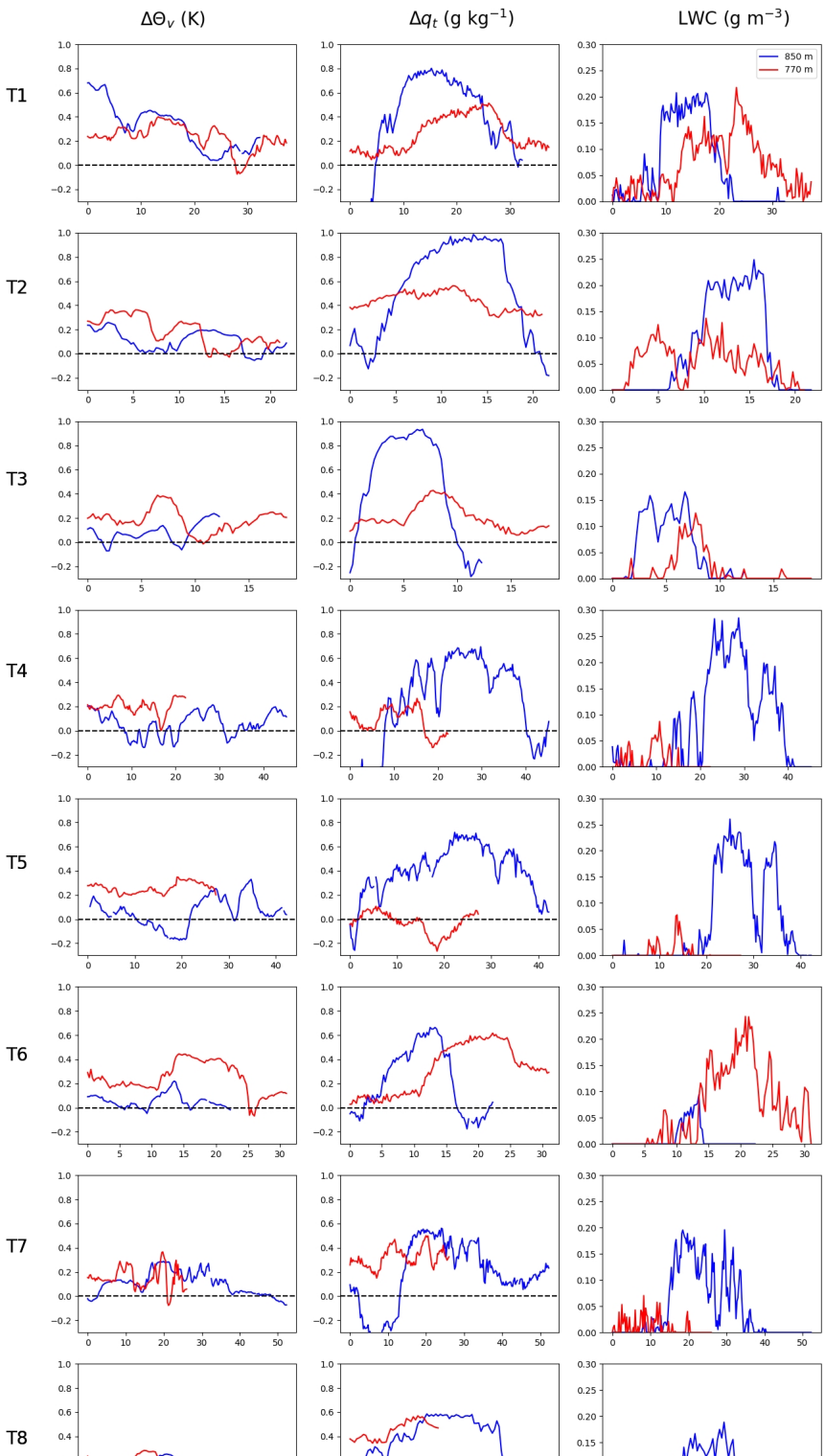
$\Delta\Theta_v$ (K)
Δq_t (g kg^{-1})
LWC (g m^{-3})
850 m
770 m
T1
T2
T3
T4
T5
T6
T7
T8